

Shear Wave Propagation in Granular Assemblies

Z. Ning¹, A. Khoubani², and T.M. Evans³

ABSTRACT

Shear wave velocity is a fundamental property of a granular assembly. It is a measure of the true elastic stiffness of a bulk specimen of discrete grains. Shear wave velocity is typically measured in the laboratory (e.g., using bender elements) or in-situ (e.g., using a seismic cone penetrometer, sCPT). In the current work, shear wave propagation is modeled numerically using the discrete element method (DEM). First, an appropriate method for measuring wave velocity is identified. The effects of particle size and elastic properties are investigated. Specimen fabric is quantified before and after wave excitation and the elasticity of the response at the scale of the particle contacts is investigated. The results show that shear wave velocity may be robustly measured for discrete numerical specimens. The ability to measure shear wave velocity using DEM simulations may provide another tool for researchers seeking to link results from physical and numerical experiments.

INTRODUCTION

The small strain shear modulus G_{max} is widely recognized as a fundamental soil stiffness property important for design and analysis of various geotechnical structures (Burland 1989; Patel et al. 2009; Clayton 2011). It is a critical input for multiple constitutive models used to describe the static and dynamic behavior of granular materials (e.g., Santamarina et al. 2001). In practice, G_{max} is normally indirectly obtained by measuring shear (S-) wave velocity V_s , which is related to G_{max} by the well-known formula:

$$G_{max} = \rho \cdot V_s^2 \quad (1)$$

where ρ is the soil bulk density (e.g., Santamarina et al., 2001).

The laboratory techniques now available to measure S-wave velocity of soils are quite diverse, such as bender element tests (Shirley and Hampton, 1978; Viggiani and Atkinson 1995; Lee and Santamarina 2005) and resonant column tests (Hardin and Richart 1963). There are also *in-situ* tests to measure V_s such as seismic cone penetration test (sCPT; Robertson et al. 1995). Among those, bender element test is the most prevailing method due to its usefulness and simplicity. A bender element is a piezoelectric transducer that can convert mechanical distortion to voltage change and vice-versa due to the phenomenon of piezoelectricity. A typical bender element test system consists of a transmitter and a

¹ Project Engineer, SOLDATA Northern America, 1448 Elliott Ave. W., Seattle, WA 98119

² Graduate Research Assistant and Jerry Yamamuro Fellow, School of Civil and Construction Engineering, Oregon State University, 101 Kearney Hall, Corvallis, OR 97331

³ Associate Professor, School of Civil and Construction Engineering, Oregon State University, 101 Kearney Hall, Corvallis, OR 97331, Corresponding author: 541.737.8535, matt.evans@oregonstate.edu

32 receiver, anchored to the top or the bottom platens of standard static testing devices (e.g. triaxial
33 apparatus and oedometer) respectively. When a voltage is applied to the transmitter, shear motions will
34 be generated and propagate through the soil and detected by the receiver. The maximum shear strain
35 induced by bender element was estimated by Dyvik and Madshus (1985) to be less than 10^{-5} . Then V_s is
36 simply calculated as the distance between the transmitter and the receiver divided by the travel time.
37 There is increasing interests in using S-wave velocity to define particle parameters (e.g. shape, elastic
38 properties, gradation; Patel et al. 2009; Yang and Gu 2012) and state (e.g. void ratio, boundary stress;
39 Hardin and Richart 1963). Another large body of research focuses on using the small strain modulus G_{max} ,
40 calculated from S-wave velocity V_s to predict the large-strain soils parameters (e.g. undrained/drained
41 shear strength; Saxena et al. 1988; Sharma et al., 2011). For all these S-wave related studies where
42 bender element tests are used, accurate determination of S-wave travel time has long been a critical but
43 controversial topic. However, due to the inherent complex particle motions, interfering side effects (e.g.
44 cross-talk; compression (P-) wave interference; Lee and Santamarina 2005) and fabrication deficiencies
45 (Montoya et al. 2013), the measurement uncertainty can lead to an error of 30-50% (Viggiani and
46 Atkinson 1995; Arroyo 2003).

47 Discrete element method (DEM) simulation is a useful tool for investigating the complex behavior of
48 particulate materials in conjunction with laboratory tests. In terms of wave propagation, two-
49 dimensional DEM simulations have been conducted to study the general relationships between wave
50 propagation variables and soil fabric (Sadd et al. 1993). Li and Holt (2002) investigated the acoustic
51 properties of weakly cemented sandstone based on elastic wave propagation using three-dimensional
52 DEM simulations. O'Donovan et al. (2012) recently used a two-dimensional DEM model with ideal
53 hexagonally-packed monodisperse discs to simulate bender element tests. This prior work demonstrates
54 the ability of DEM simulations to capture the parameters of interest which are difficult or very expensive
55 to directly observe in standard physical tests.

56 The object of this work is to study both specimen-scale and particle-scale responses of three-
57 dimensional granular assemblies during S-wave propagation in an environment which is similar to the
58 physical bender element test, so as to provide insights for the design of physical experiments and
59 potentially a more robust linkage between physical and numerical experiments. The simulation of DEM
60 specimen, S-wave generation and measurement are presented first, followed by an examination of
61 system response at the particle level. Receiving signals from multiple receivers were interpreted with
62 different methods. Finally the effects of excitation signals, particle properties and stress state on S-wave
63 velocity are analyzed.

64 **SIMULATION OF SHEAR WAVE PROPAGATION**

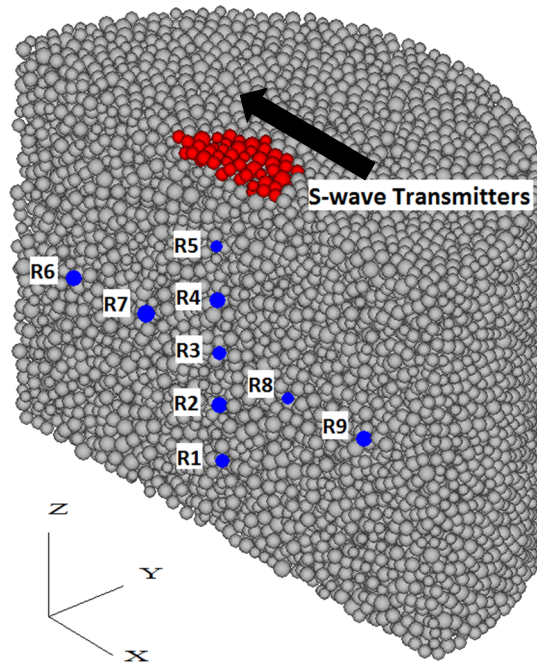
65 **Specimen Generation**

66 Shear wave propagation was simulated using the DEM program *PFC^{3D}* (Itasca 2009). Cylindrical DEM
67 specimens having a diameter (D) to height (H) ratio of 3:2 were modeled. The high D/H ratio was
68 employed to minimize boundary effects and compression (P-) wave reflection observed in assemblies
69 having typical (i.e., D/H = 0.5) triaxial specimen geometry. Particles were simulated as spheres with
70 Hertz-Mindlin contacts. A typical specimen consists of approximately 52,000 particles. Two planar rigid

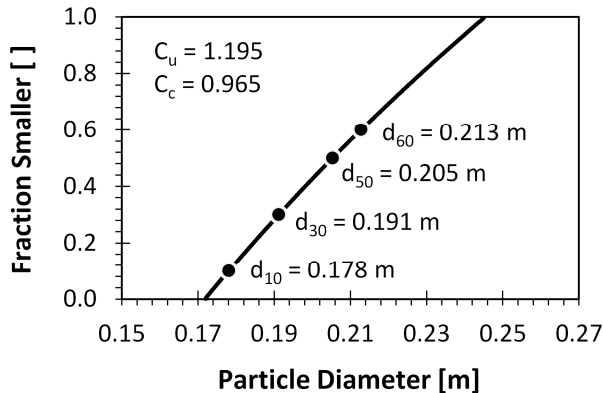
71 walls defined the top and bottom boundaries of the specimen and were used to control the applied
72 vertical stress. Radial confinement was supplied by stacked cylindrical walls to simulate a flexible
73 membrane (Zhao and Evans, 2009). The basic DEM model properties and S-wave measurement
74 parameters are listed in Table 1. Some of these properties were subsequently varied as part of a
75 parametric study. In order to increase the allowable solution time increment, mass scaling of 1000:1 was
76 used. In this type of scaling, particle sizes are increased while particle densities remain constant. It has
77 been shown that mass-scaled DEM simulations reasonably mimic microscale evolution in real granular
78 materials (Evans and Frost 2007; Belheine et al., 2009; Evans and Frost, 2010; Evans and Valdes, 2011).
79 Simulations were conducted in the absence of gravity to prevent body force-induced stress gradients
80 from arising due to the scaled particle sizes.

81 **Table 1.** Basic DEM model properties and S-wave measurement parameters

Parameters	Value
Particle properties	
Contact Model	Hertz-Mindlin
Specific gravity, G_s	2.65
Particle shear modulus, G_g	2.9×10^9 Pa
Particle Poisson's ratio, ν_g	0.31
Interparticle friction coefficient, μ	0.31
Mean particle diameter, d_{50}	0.205 m
Uniformity coefficient, C_u	1.2
Specimen geometry	
Specimen diameter/ d_{50}	43.9
Specimen height/ d_{50}	29.3
S-wave measurement parameters	
Confining stress	150 kPa
Excitation amplitude/ d_{50}	5×10^{-5}
Excitation frequency	50 Hz



(a)



(b)

82

83

84

85

86 **Figure 1.** (a) A typical DEM specimen with S-wave transmitting zone and receivers (R1, R2, R3, R4 and R5 are
 87 primary receivers; R6, R7, R8 and R9 are complementary receivers. For clarity, only half of the specimen.).
 88 (b) Grain size distribution of specimen.

89 **Shear Wave Generation and Receiving**

90 S-waves were generated by applying a horizontal excitation to a thin layer of particles at one end of the
 91 specimen using a single sinusoidal velocity pulse. The DEM models can be excited by sine pulses with
 92 different frequencies to approximately identify the resonant frequency (Ning and Evans, 2013). The
 93 excitation frequency was selected near the resonant frequency to obtain strong frequency response in
 94 the model. The diameter of this S-wave transmitting zone is $D/4$ (D = specimen diameter) and its
 95 thickness is nominally $2 \times d_{50}$ (i.e., it is comprised of particles whose centroids lie within $1.5 \times d_{50}$ of the top

96 of the specimen). Compared to the S-wave generation by bender elements, in which the wave source is
97 a point and the wave propagation front is spherical, this approach reduces the P-wave interference
98 effect (Lee and Santamarina 2005) observed in physical specimens (Ning and Evans 2013).

99 In a physical test, bender elements are typically installed on the boundary of a specimen (e.g., the end
100 platens of a triaxial device or oedometer cell), which makes it difficult to access the information within
101 the specimen – that is, the measured shear wave velocity will be a spatially averaged quantity over the
102 height of the specimen. In DEM simulations the displacement and velocity of each individual particle is
103 known, allowing for multiple wave receivers at specified locations to monitor particle motions during
104 wave propagation. In the current study, five approximately equally spaced particles along the central
105 axis of the cylindrical specimen were selected as primary S-wave receivers (R1-R5, Figure 1). In addition,
106 four complementary receivers (R6-R9) were defined on a line orthogonal to the z-axis and parallel to the
107 direction of shear excitation (i.e., the x-axis). Multiple receivers allow for a wider variety of procedures
108 to interpret S-wave velocity.

109 **Simulation Process**

110 Simulation of shear wave propagation consists of the following: (1) specimen generation; (2) pre-
111 excitation preparation; and (3) shear wave transmission and measurement.

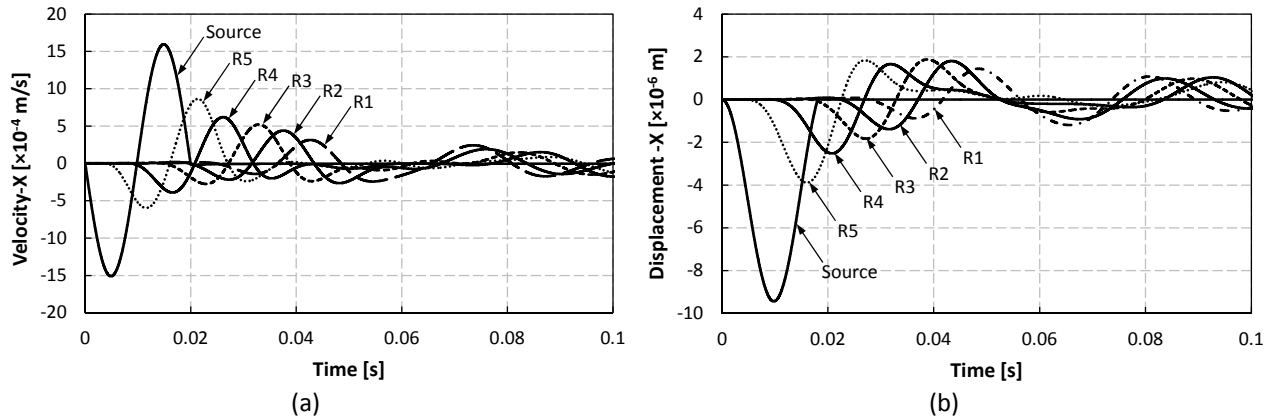
112 In step one, the DEM specimen was assembled with a predefined void ratio and isotropically
113 consolidated to a certain stress state. In step two, the model was cycled with high local damping to
114 ensure that pre-excitation particle motions are negligible compared to post-excitation particle motions.
115 Once all particles in the assembly are sufficiently still, the local damping ratio is returned to a physically
116 realistic value. Finally, a sinusoidal velocity pulse with pre-defined amplitude, frequency, and duration
117 was applied to the particles located in the shear-wave transmitting zone. The displacement and velocity
118 of the receivers were monitored.

119 Energy is dissipated in DEM simulations via frictional sliding and contact dissolution. However, because
120 the contact laws used in the current simulation are purely elastic, there is no asperity yield at particle
121 contacts (O’Sullivan 2011). Therefore, the amount of energy dissipated may not be sufficient to prevent
122 non-physical vibrations in the particles (Itasca 2009). In the current work, viscous damping was used to
123 prevent unrealistic particle motion.

124 **Signal Analysis**

125 Figure 2 shows the source and receiving signals in terms of the x component of displacement and
126 velocity (i.e., in the direction that the particles in the transmitting zone were excited) from a single
127 typical S-wave propagation simulation. The signals as recorded at the receivers are designated *R1* to *R5*
128 (from the furthest to the nearest transmitter, respectively) while *S* denotes the source signal. Unlike
129 most receiving signals obtained in laboratory bender element tests (e.g. Viggiani and Atkinson 1995),
130 these signals are very ‘clean’ because they are free of many factors which may exist in laboratory tests
131 such as cross-talk, electromagnetic noise, and background mechanical vibration (Lee and Santamarina
132 2005; Montoya et al. 2012). This high signal quality results in particularly robust determinations of travel
133 time. Moreover, results of bender element test are in terms of displacement; however, in the numerical

134 model there is access to the receivers' displacement and velocity. Both displacement and velocity signals
135 were used for determining a more precise shear wave velocity, as explained below.



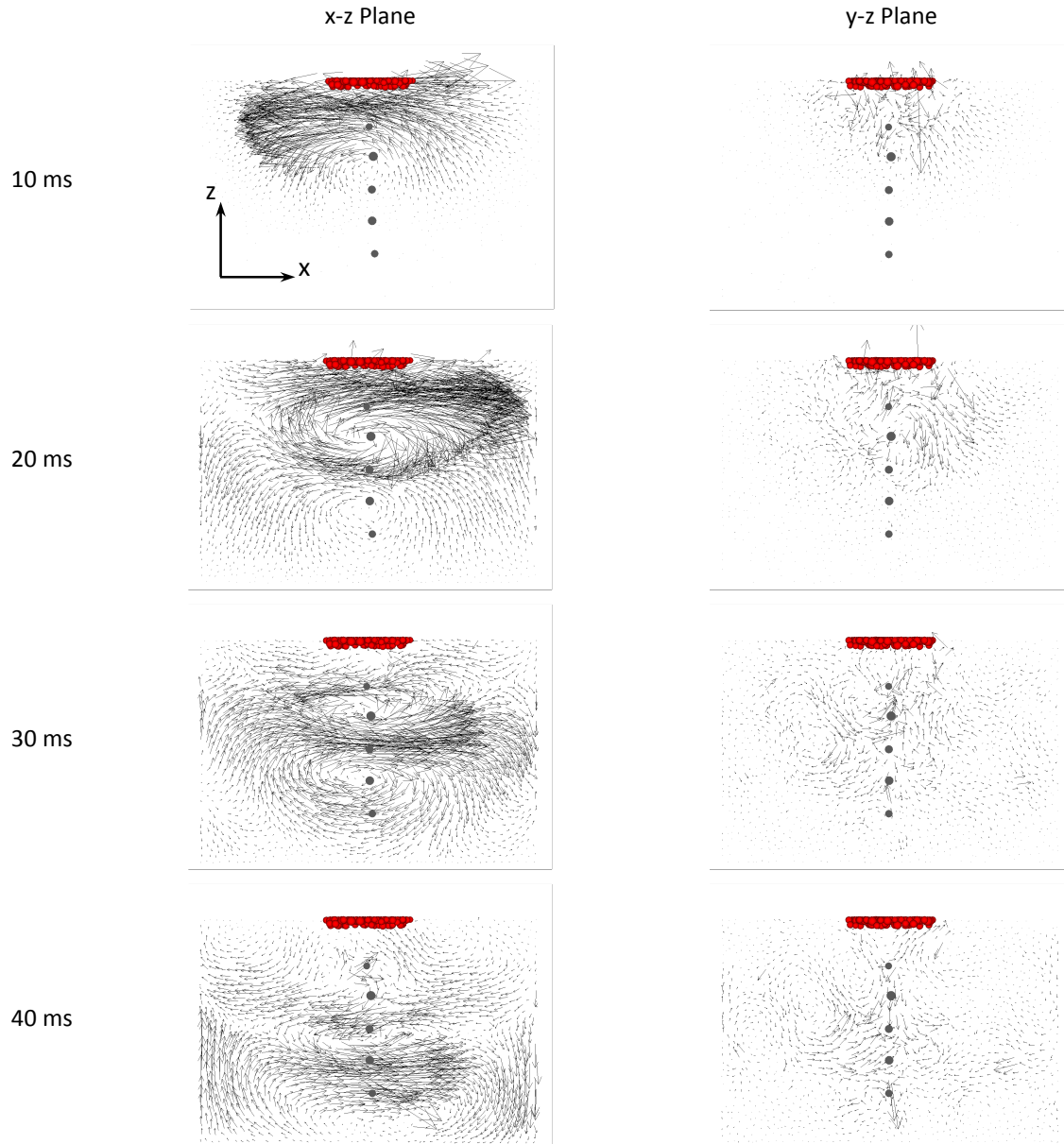
136 **Figure 2.** Transmitting and receiving signals for S-wave velocity measurement. **(a)** x-velocity response; **(b)** x-
137 displacement response

138 The source velocity signal shown in Figure 2(a) is a single-period sinusoidal pulse, which coincides with
139 the input shear wave parameters. The source displacement signal shown in Figure 2(b) basically matches
140 the integration of the source velocity signal over the duration of the transmitting signal, showing the
141 particles in the transmitting zone were first moved in the -X direction and then moved back to their
142 original location. In both the velocity and displacement signals, it can be seen that the receivers at
143 different locations respond to the excitation at different times (from the earliest to the latest: R5, R4, R3,
144 R2, R1). The delays of the receiving signals between equally spaced receivers are almost the same and
145 the receiving signals attenuate as the distance from the source increases. The receiving signals also
146 indicate reflection at the bottom boundary of the specimen. From around 0.06-0.08 s, it can be seen
147 that the receivers' responses – which had already been attenuated – again increased but in an inverted
148 sequence: the closer to the base of the specimen, the earlier the response (from the earliest to the
149 latest: R1, R2, R3, R4, R5).

150 EXAMINATION OF SYSTEM RESPONSE

151 DEM simulations allow for both particle-level and specimen-level analyses. The evolution of the particle
152 velocity vector field and local strain contours are used to analyze the complicated system response
153 during shear wave propagation and also to help to correctly interpret the wave receiver signals in order
154 to determine S-wave velocity. Figure 3 shows the evolution of instantaneous particle velocity vectors
155 during S-wave propagation at four successive time points (10, 20, 30, and 40 ms after excitation) on the
156 x-z and y-z planes shown in Figure 1. The particle velocity vectors are plotted in Figure 3 with their
157 length proportional to the magnitude of velocity (the largest vector corresponds to a velocity of 3×10^{-4}
158 m/s). These four snapshots of particle velocity vectors combined with the receiving signals in time
159 domain shown in Figure 2 demonstrate the interplay between particle-scale and specimen-scale
160 behavior as the S-wave propagates through the specimen.

161



162 **Figure 3.** Instantaneous particle velocity vectors on x-z and y-z planes at 10, 20, 30, and 40 ms after excitation.
 163 Transmitter particles are shown in red while the five primary receiver particles are shown in grey. Note that all
 164 velocity arrows are plotted at the same scale.

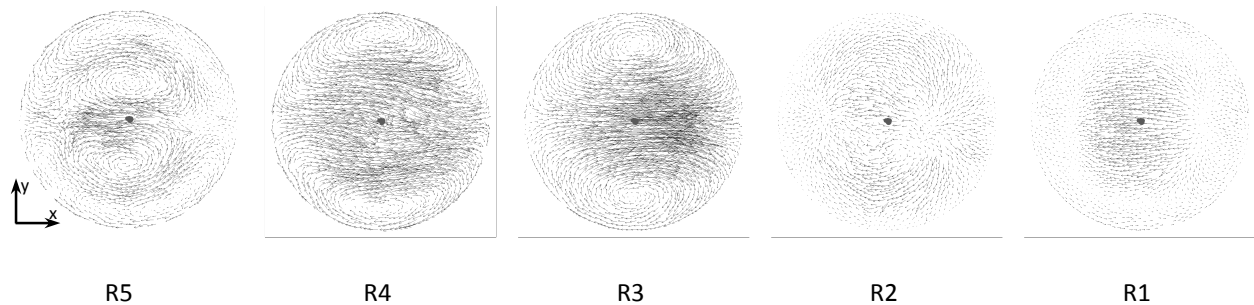
165 At 10 ms, as shown in Figure 2, the velocities of S-wave transmitting particles are zero and their
 166 displacements reach the peak value in the x-direction. Receiver *R5* has moved towards the x-direction
 167 while receiver *R4* remained quiet. In Figure 3, strong horizontal particle motions in the x-direction are
 168 indicated by the velocity vectors in the zone between the S-wave transmitting zone and receiver *R5*. It
 169 can also be observed that to the left of the zone in front of the shear motion, particles have a tendency
 170 to move downwards while to the right of the zone in front of shear motion, particles have a tendency to
 171 move upwards, which forms a vortex-like disturbance ahead of the main shear motions. These vortices
 172 bear some resemblance to the experimental and numerical observations of others (e.g., Rechenmacher
 173 2006; Tordesillas et al., 2008), but the underlying mechanics are fundamentally different. Specifically,

174 Tordesillas et al. (2008) noted that the emergence of vortices (along with so-called microbands) as the
175 predominant mode of nonaffine deformation were an indicator of impending shear band formation
176 coinciding with peak stress ratio. With respect to wave propagation, however, there is no large-scale
177 failure impending. Nonetheless, the observed vortices correspond with unjamming events (i.e., initiation
178 of particle motion from an initially jammed state) and are associated with very small, local deformations,
179 similar to observations reported by Tordesillas et al. (2008).

180 At 20 ms, the transmitting particles have moved back to their original position. Figure 3 shows the first
181 S-wave lobe (-x) has reached receiver *R3* and a new S-wave lobe in the opposite direction (+x) exists and
182 approaches receiver *R4*. These two S-wave lobes form a vortex in the zone between receivers *R5* and *R3*.
183 At 30 ms, the first S-wave lobes (-x) have reached the farthest receiver but are greatly attenuated. The
184 second S-wave lobe (+x) has passed receiver *R3*. And a third S-wave lobe (-x) has been generated and
185 has reached receiver *R5*. These three S-wave lobes form two vortices as clearly shown in Figure 3 on the
186 x-z plane at 20 ms and 30 ms after initiation. Finally, at 40 ms, the first S-wave lobe vanishes. The second
187 and the third S-wave lobes have proceeded to receiver *R1* and receiver *R3*, respectively. No appreciable
188 new S-wave lobe is generated after the third lobe.

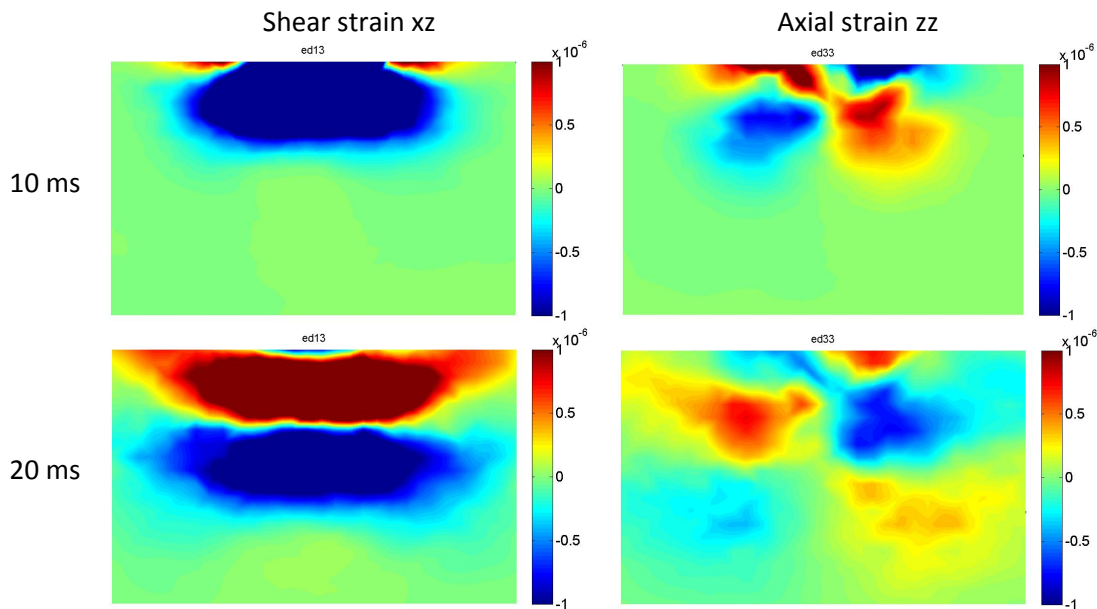
189 On the y-z plane, the arrows of velocity vectors are much shorter than those on the x-z plane (Figure 3),
190 indicating that the main particle motions occur in the direction perpendicular to this plane. However,
191 small disturbances can still be observed near the axis of the specimen. The zone of disturbance
192 progresses as the S-wave propagates through the specimen.

193 To illustrate the complicated three-dimensional nature of the particle motions, the particle velocity
194 vectors at 30 ms on five cutting planes going through the five primary receivers, respectively, with their
195 normal parallel to the z-axis are shown in Figure 4. The particle motions shown in Figure 4 are consistent
196 with the observations made from Figure 3. Horizontal motions in the negative x-direction are seen on
197 plane x-y-*R1* (the first S-wave lobe) and plane x-y-*R5* (the third S-wave lobe). Stronger positive-x
198 horizontal motions (the second S-wave lobe) occur on plane x-y- *R3* and plane x-y-*R4*. The main shear
199 motions are limited to a central circular zone with a diameter of approximately one-half the diameter of
200 the specimen. Vortices are also observed on plane x-y-*R5*, x-y-*R4* and x-y-*R3*. As clearly shown on plane
201 x-y-*R5*, two vortices are formed symmetrically on each side of the main zone of perturbation.



202 **Figure 4.** Particle velocity vectors on x-y planes at 30 ms, through each receiver. Note that the scale for the velocity
203 vectors is the same as in Figure 3.

204 The upward and downward particle motions observed in Figure 3 imply coupled P-S-wave propagation
 205 in the specimen. To better study this phenomenon, both shear strain (ϵ_{xz}) and axial strain (ϵ_{zz}) contours
 206 on x-z-plane at 10 ms and 20 ms are shown in Figure 5. Local strain is calculated from volume-averaged
 207 measurements of strain rate and the current time step for the simulation. In Figure 5, shear strains are
 208 clearly shown in the zones where large horizontal motions occur as indicated in the velocity vectors field.
 209 The formation, progression and vanishing of the shear strain localization zones exactly coincide with the
 210 shear wave lobes shown above in Figure 3. In Figure 5, a P-wave is also illustrated by the alternating
 211 contractive and dilatant local strains, which are antisymmetric with respect to the central axis.
 212 Comparing shear strain to axial strain, it is clear that the P-wave propagates faster than the S-wave.

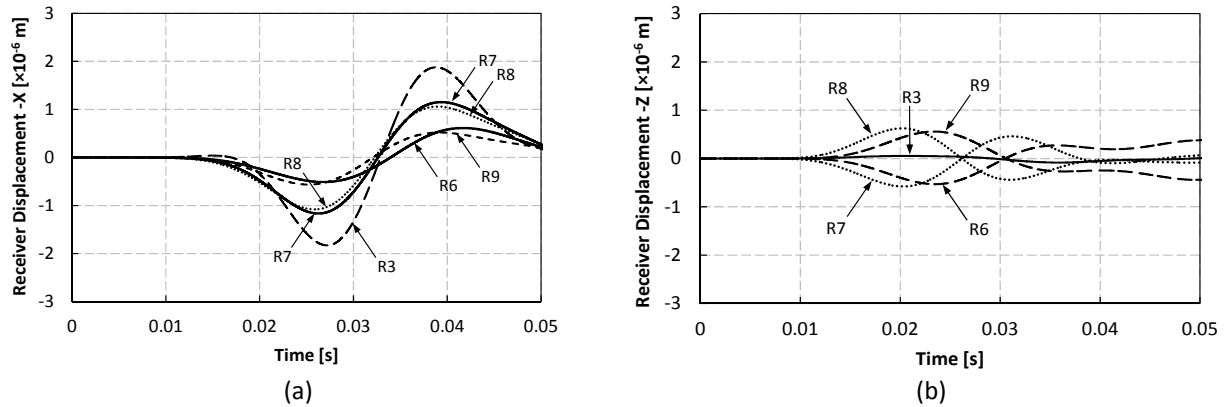


213 **Figure 5.** Contours of shear strain-xz and axial strain-zz on xz-plane at 10 ms and 20 ms.

214 To examine the effects of P-wave interference on S-wave velocity measurements, displacements in the x
 215 and z-directions of primary receiver *R3* and the four complementary receivers *R6*, *R7*, *R8* and *R9* are
 216 measured and shown in Figure 6. The five receivers have approximately the same distance to the S-wave
 217 transmitting zone. They are symmetric to the central axis and equally spaced (with *R3* in the middle).

218 Figure 6(a) shows that receivers symmetric to the axis have a similar x-displacement response, such as
 219 *R6/R9* and *R7/R8*. The larger the distance to the axis, the smaller the amplitude of receiving signal.
 220 Receiver *R3*, which is located at the axis, has the greatest response. In Figure 6(b), *R6/R9* and *R7/R8*,
 221 have similar but inverse z-displacement receiving signals. Receivers *R6* and *R7* are at the zone showing
 222 downward velocity vectors when the first S-wave is approaching (Figure 3), so the initial polarity of
 223 receiving signals is negative as shown in Figure 6(b). Similarly, *R8* and *R9* are at the zone showing
 224 upwards velocity vectors when the first S-wave is approaching, thus showing positive initial polarity. In
 225 Figure 6(b), the receiver to axis distance has little effect on the amplitude of the receiving signals but
 226 affects the arrival time. It should be noted that *R3* has nearly zero z-displacement response which
 227 implies a smaller P-wave inference along the axis. Thus, P-wave inference does exist when a specimen is

228 subjected to S-wave excitation, but if the specimen boundaries are sufficiently distant, the zone along
229 the central axis is less affected by P-wave inference.



230 **Figure 6.** Receiving signals in terms of: (a) displacement in x direction; (b) displacement in z direction.

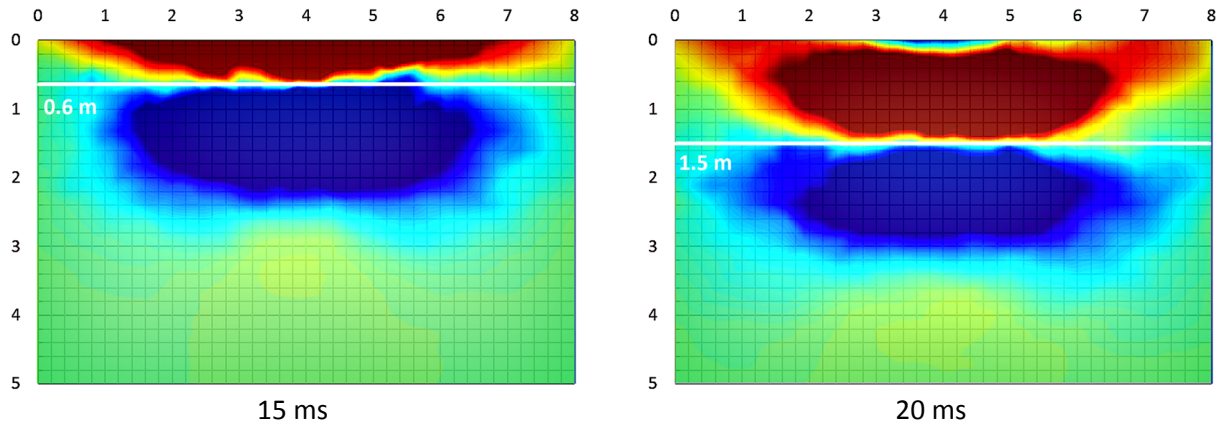
231 INTERPRETATION OF RECEIVED SIGNAL

232 In physical bender element tests, S-wave velocity is calculated from the travel time and the distance
233 between the source and the receiver. The start-to-start and peak-to-peak methods (Viggiani and
234 Atkinson 1995) are often used. In the current simulations, the multiple-receiver configuration makes it
235 possible to calculate S-wave velocity from the travel time and the distance between receivers. Note in
236 Figure 2, though the receiving signals resemble the source signal, there is a higher level of similarity
237 amongst the receiving signals. Key features of the waveform such as the start and peak points are clearly
238 defined in the numerical receiving signals due to their noise-free quality, which to a great extent
239 reduces the uncertainties associated with determining S-wave velocity.

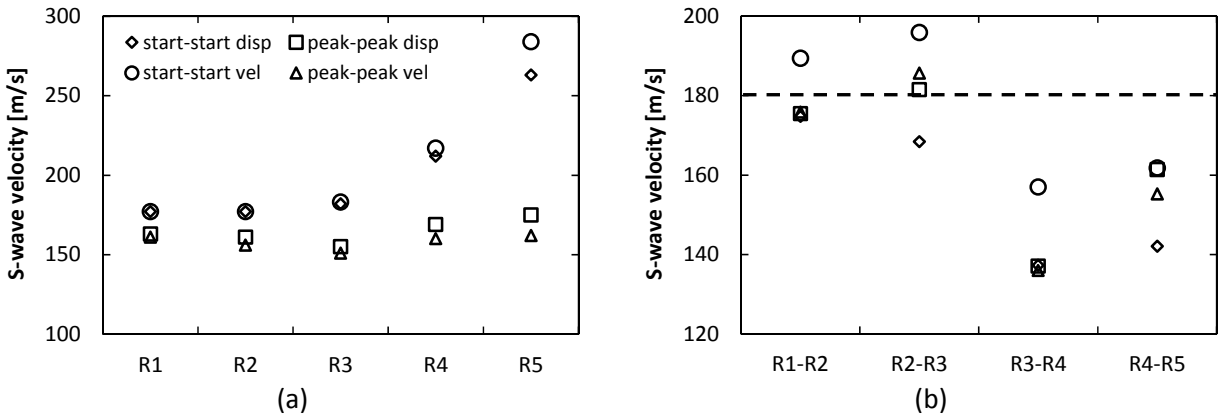
240 In Figure 5, since the shear strain contours can be determined directly from the DEM simulations, they
241 provide a fundamental approach for determining S-wave velocity as shown in Figure 7. In Figure 7, a
242 square grid is placed on the shear strain contours so the travel distance of the shear wave at different
243 time points can be accurately measured. Then the S-wave velocity can be readily obtained by dividing
244 the travel distance by the time difference. In Figure 7, because the front edge of the first shear lobe (in
245 blue) is not very clearly defined, the front edge of the second shear lobe (in red) was used as a reference.
246 It reached 0.6 m and 1.5 m at 15 ms and 20 ms respectively after excitation. So the S-wave velocity is:
247 $(1.5 \text{ m} - 0.6 \text{ m}) / (20 \text{ ms} - 15 \text{ ms}) = 180 \text{ m/s}$. This value will be used as a baseline value to examine the
248 validity of other signal-based S-wave determination methods that follow.

249 Figure 8(a) shows S-wave velocities calculated between the source and each of the five primary
250 receivers and Figure 8(b) shows S-wave velocities calculated between four pairs of neighboring primary
251 receivers based on both x-displacement and x-velocity signals. In general, the S-wave velocities
252 calculated by different methods based on both displacement and velocity signals are consistent for
253 receivers *R1*, *R2*, and *R3*. Due to near field effects (Sanchez-Salinerio et al. 1986; Arroyo 2003), the S-
254 wave velocities calculated from receivers *R4* and *R5* are relatively higher than average (which also
255 affects the accuracy of S-wave velocities determined between pairs *R3-R4* and *R4-R5*). The S-wave
256 velocities determined using the start-to-start method between source and receivers is generally higher

257 than those determined using peak-to-peak method as shown in Figure 8(a). This variation is due to the
 258 fact that the receivers do not necessarily respond at the same excitation frequency that the source
 259 particles do (thus the lags between the start point and the peak point could be different), which is
 260 further discussed below. In the following discussion, S-wave velocity will be determined by averaging
 261 the results obtained using receiver to receiver analysis from receiver pairs *R1-R2* and *R2-R3* based on the
 262 peak to peak method. This averaged S-wave velocity for the case shown in Figure 8 is 180 m/s. This is
 263 consistent with the baseline S-wave velocity determined based on shear strain contours in Figure 7.



264 **Figure 7.** Determining travelling distance of shear wave based on graduated shear strain contours.

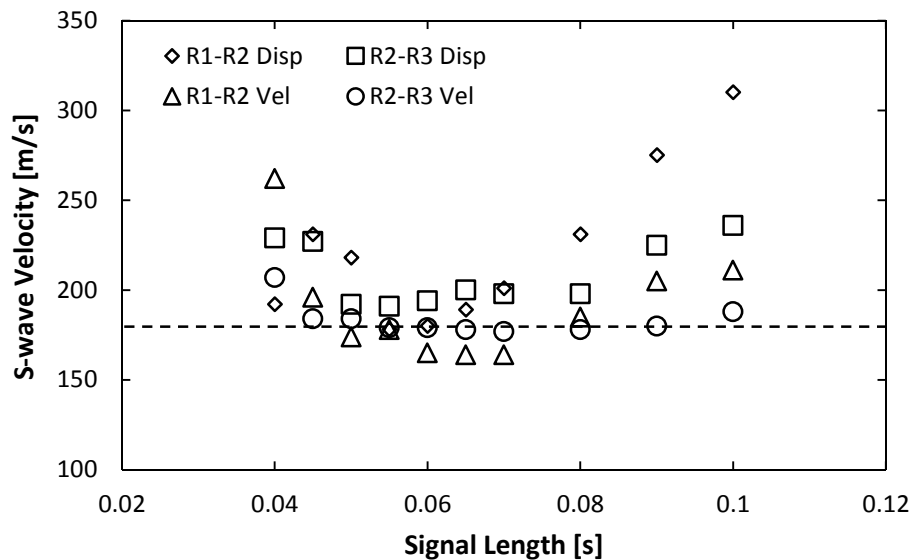


265 **Figure 8.** V_s determined by different methods. (a) source to receivers analysis; (b) receiver to receiver analysis

266 Another commonly used method to determine S-wave velocity in the time domain is cross-correlation
 267 (Viggiani and Atkinson 1995), a signal processing operation used to identify similarities between two
 268 time-shifted signals (Santamarina and Fratta, 2005). When it is applied to the bender element test, the
 269 waveforms of the two signals are required to be highly similar so as to effectively determine the S-wave
 270 travel time, yet this is not always well satisfied between a source signal and a receiving signal in a
 271 physical test. In DEM simulations, cross-correlation can be readily applied between any two receivers.
 272 Cross-correlation is useful in automating the S-wave velocity calculation, especially when continuous
 273 measurement is required.

274 The length of the signal used to perform cross-correlation has a significant effect on the results, which
 275 has been seldom discussed in previous studies. To study the effect of signal length, cross-correlation was

276 performed on receiver pairs *R1-R2* and *R2-R3* based on both *x*-displacement and *x*-velocity signals with
 277 various signal lengths from 0.04-0.10 s. The calculated S-wave velocities based on the travel time
 278 determined from cross-correlation are shown in Figure 9. As shown in Figure 9, a significant variation
 279 was observed when different signal lengths were used. The cross-correlation method over predicted the
 280 S-wave velocity when either the signal length is too short or too long. The largest error is 88% compared
 281 to the baseline value when the signal length is 0.1 s. The calculated S-wave velocities are consistent with
 282 the reference value when the signal length is 0.055-0.060 s. This can be explained by noting that 0.055-
 283 0.060 s is approximately the time it takes for the S-wave to reach the bottom boundary of the specimen
 284 before reflection occurs. Receiving signals longer than 0.06 s contain information of the reflecting wave
 285 while short receiving signals contains incomplete information; either case can lead to misinterpretation
 286 of the S-wave travel time. Therefore, the length of signals should be carefully selected when using cross-
 287 correlation to determine S-wave velocities.



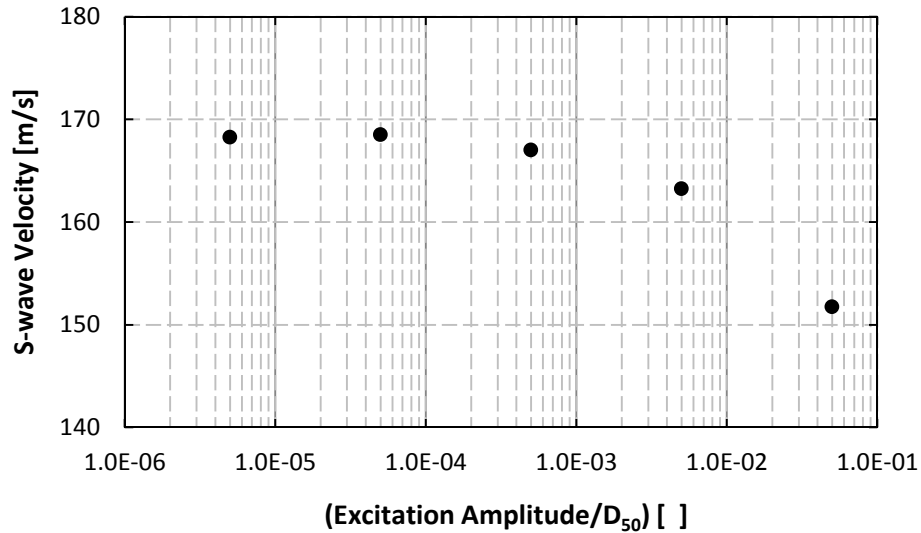
288 **Figure 9.** Effect of signal length on S-wave velocity determination by cross-correlation. The average S-wave velocity
 289 from start-start and peak-peak measurements is shown as a horizontal dashed line for comparison.
 290

291 EFFECTS OF EXCITATION SIGNAL

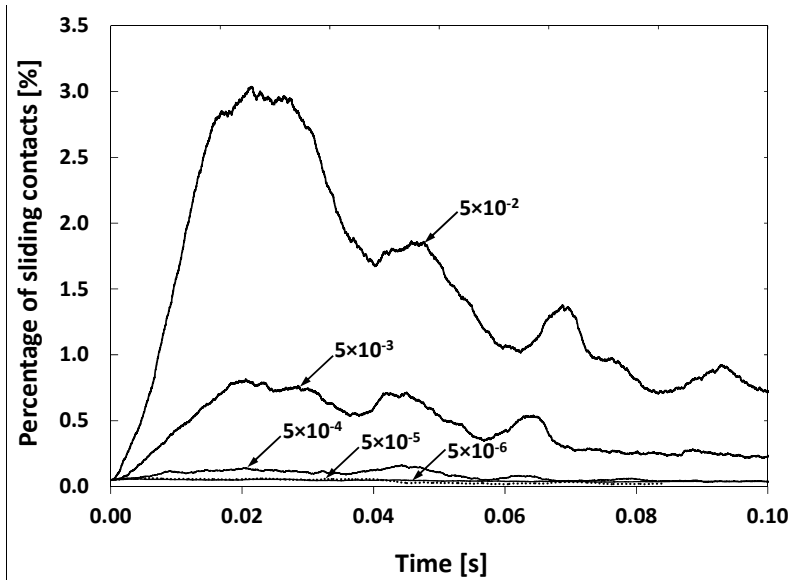
292 Effects of excitation amplitude

293 As noted above, the shear stiffness of granular material is a function of strain level, thus the S-wave
 294 velocity varies as it is measured at different strain levels. In laboratory bender element tests, the shear
 295 strain induced in the specimen is controlled by the amplitude of the excitation signal. In the current
 296 study, a series of simulations were performed with various excitation amplitudes ($\text{amplitude}/D_{50} = 5 \times 10^{-6} \sim 5 \times 10^{-2}$)
 297 and the S-wave velocities were determined and are shown in Figure 10. It is seen that S-wave
 298 velocity is constant when the amplitude/ D_{50} ratio is low ($< 1 \times 10^{-4}$) and then decreases as the excitation
 299 amplitude is further increased. Similar observations were have been made from bender element test
 300 results (Montoya et al 2013). The degradation in inter-particle stiffness and thus, the S-wave velocity, is
 301 due to the transition from elastic to plastic behaviors at contact (i.e., contact slip) (Santamarina et al.
 302 2001; Agnolin and Roux 2007). In the current study, contact slip was monitored within the DEM

303 specimen as shown in Figure 11. Figure 11 shows the fraction of contacts where slip is occurring during
 304 the first 100 ms of wave propagation ($\Delta t = 1 \mu s$). Small normalized excitation amplitudes (i.e., 5×10^{-6} and
 305 5×10^{-5}) have almost the same slip fraction, which is consistent with the computed shear wave velocity
 306 values shown in Figure 10 for these two excitation amplitudes (i.e., they are very similar). The sliding
 307 fraction for a normalized amplitude of 5×10^{-4} shows a slight increase compared to the smaller
 308 normalized amplitudes, which explains the small decrease in shear wave velocity value shown in Figure
 309 10. Further increases of normalized amplitude result in considerable increases in the sliding fraction,
 310 which are accompanied by considerable decreases in shear wave velocity, as shown in Figure 10.



311
 312 **Figure 10.** S-wave velocity versus excitation amplitudes



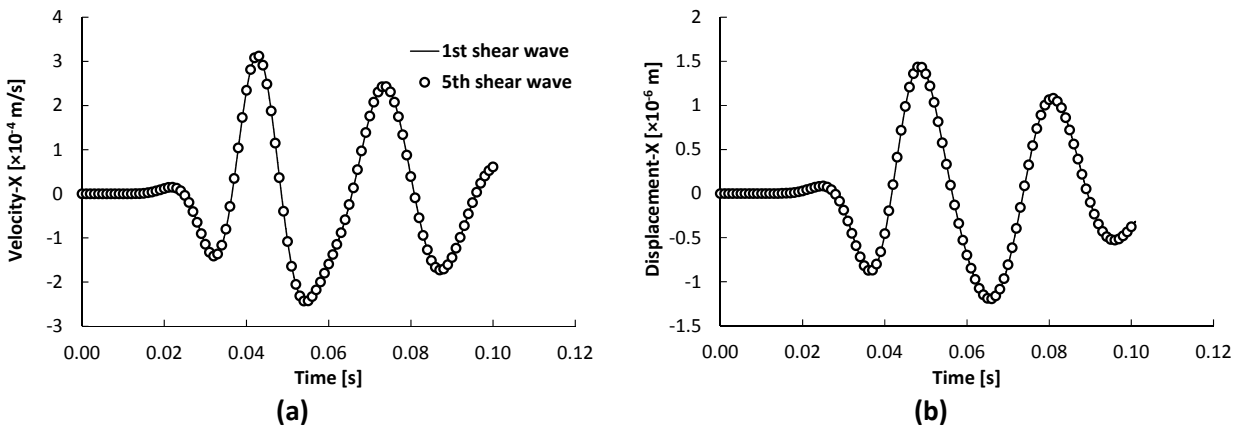
313
 314 **Figure 11.** Percentage of sliding contacts for different values of Amplitude/d₅₀

315 **Verification of Elasticity**

316 The previous section shows the importance of excitation amplitude in determining shear wave velocity.
317 Specifically, care should be taken when choosing the excitation amplitude to avoid plastic response at
318 particle contacts. To ensure that the particle assembly is elastic under shear wave excitation, five shear
319 waves with an amplitude/ D_{50} equal to 5×10^{-5} were applied to the assembly and time history responses
320 of each receiver for different shear waves were recorded. If the amplitude of the shear stress passing
321 through the soil is large enough to cause rotation or sliding of particles, the soil fabric is altered and
322 different responses will be expected for successive application of shear waves. Figure 12 shows the
323 horizontal velocity and displacement time histories of receiver R1 during application of the first and fifth
324 shear waves. It can be seen that the time histories match each other, indicating of elastic behavior.
325 Therefore, this amplitude is used throughout this study for determination of shear wave velocity. This
326 result is consistent with Figure 10 which shows a constant shear wave velocity for an excitation
327 amplitude/ D_{50} ratio less than 1×10^{-4} .

328 To investigate elasticity at the microscale, spherical histograms were used to describe the three-
329 dimensional spatial distribution of contact orientation, normal force, and shear force in the particulate
330 assembly as shown in Figure 13. The normalized amplitude of the applied shear wave was 5×10^{-5} . For
331 contact orientation, the radius of the spherical histogram for a given solid angle $d\Omega$ is the total number
332 of contacts within $d\Omega$ normalized by the total number of contacts in the assembly. For normal and shear
333 force, the radius of the spherical histogram for a given solid angle $d\Omega$ is the ratio of the mean of the
334 contact normal or shear forces having orientations within $d\Omega$ normalized by the mean contact normal
335 force in the assembly. It is observed that all the histograms are the same during the application of shear
336 wave, indicating assembly's fabric remains unchanged.

337

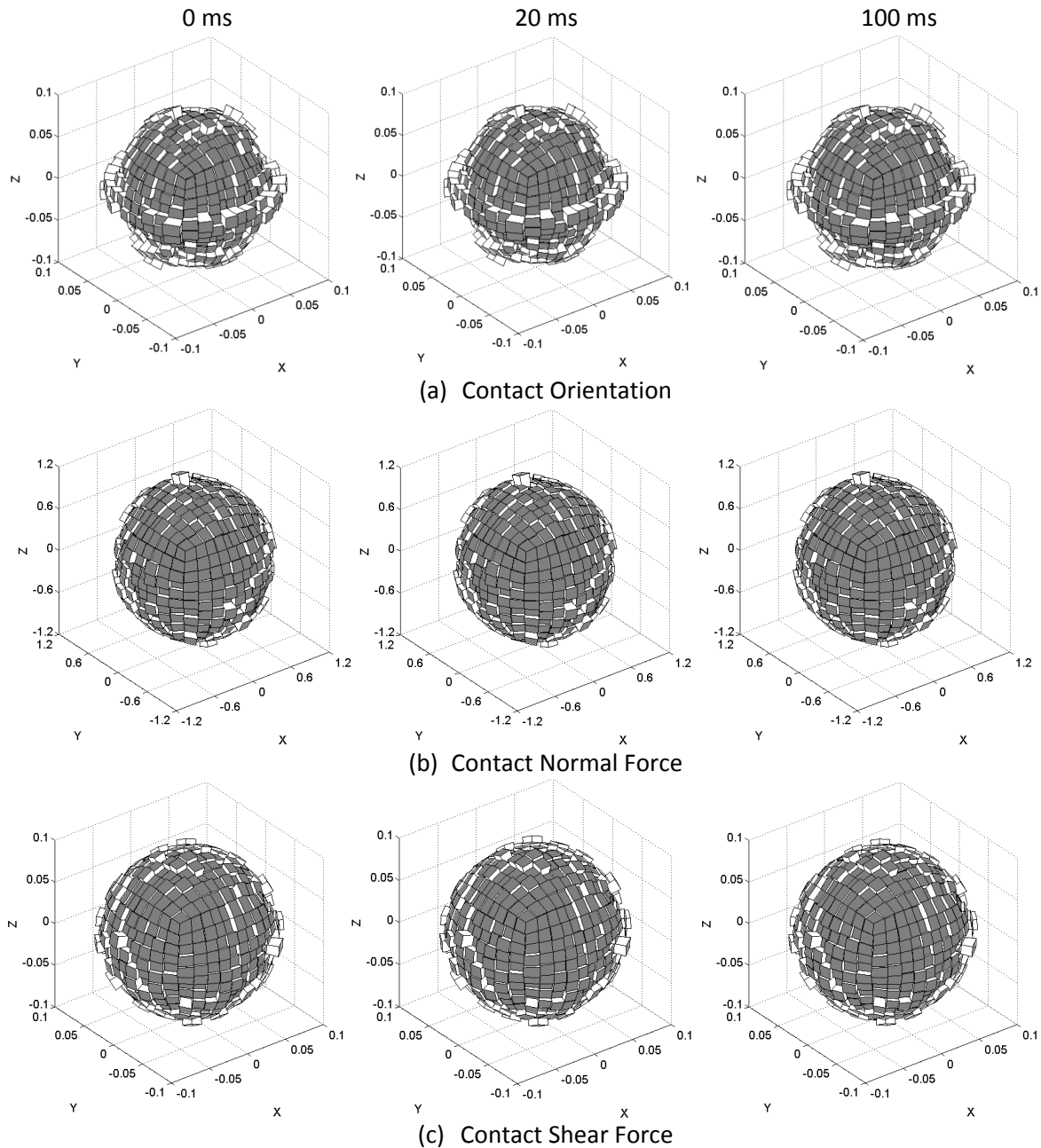


338 **Figure 12.** Comparison of horizontal (a) velocity and (b) displacement time histories recorded at receiver R1 during
339 application of first and fifth shear waves.

340 **EFFECTS OF PARTICLE SIZE**

341 The effect of particle size on S-wave velocity has been widely studied by using bender element tests.
342 Recent work by Yang and Gu (2012) found contradictory results when comparing results of previous
343 researchers. DEM simulation allows for the study of particle size effect with a much larger size range

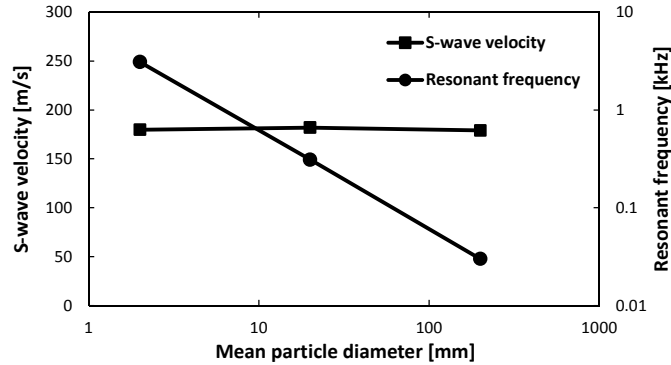
344 than physical test does. Knowledge of the particle size effects on wave propagation is important for
 345 DEM simulations to assess the validity of mass-scaling to decrease computation time (e.g. Evans and
 346 Frost 2007, Jacobson et al. 2007, Belheine et el. 2009).



347 **Figure 13.** Spherical histogram of (a) contacts' orientation; (b) contacts' normal force; (c) contacts' shear force
 348 during application of shear wave velocity (Normalized amplitude = 5×10^{-5}).

349 Three mean particle sizes were considered (2 mm, 20 mm, and 200 mm). The number of particles was
 350 kept constant and only particle size was changed. Since wave propagation is a dispersive phenomenon
 351 involving high frequency effects, different responses are expected from models with different particle
 352 sizes. Figure 14 shows the effects of particle size on S-wave velocity and resonant frequency. There was

353 little change in S-wave velocity over two orders of magnitude in particle size. This agrees with results
 354 presented by Yang and Gu (2012), who found that S-wave velocity is effectively size independent.
 355 Regarding the resonant frequency of the model, power law behavior was observed. These results
 356 indicate that mass-scaling (which is used in current study) can be applied to reduce computing time in
 357 DEM simulations of S-wave propagation without altering the simulated S-wave velocity. The excitation
 358 frequency should be carefully selected near the resonant frequency (a function of the particle size) to
 359 obtain strong frequency response in the model.



360
 361 **Figure 14.** Effects of particle size on S-wave velocity and resonant frequency.

362 **EFFECTS OF STRESS STATE AND PARTICLE MATERIAL PROPERTIES**

363 Stress state affects interparticle stiffness (e.g., Santamarina et al. 2001) and, perhaps more significantly,
 364 contact quality (Evans et al. 2011) and thus, wave propagation speed. Experimental evidence and
 365 analytical studies support the choice of a power function to relate velocity and effective mean stress, p' ,
 366 which can be expressed as:

367
$$V_s = \alpha \left(\frac{p'}{1 \text{ kPa}} \right)^\beta \quad (2)$$

368 where α and β are fitting parameters. α represents the S-wave velocity under 1 kPa effective mean
 369 stress and β reflects the sensitivity of the S-wave velocity to the change in effective mean stress. Both α
 370 and β vary with the particle material properties, contact behavior and packing. The Hertzian contact
 371 model used in the current study is defined by two material properties: particle shear modulus G_g and
 372 particle Poisson's ratio ν_g . Interparticle secant normal stiffness using the Hertzian contact model is
 373 defined as:

374
$$k_n = \frac{2G_g \sqrt{2R}}{3(1-\nu_g)} \sqrt{U} \quad (3)$$

375 where U is the overlap of the two particles (the so-called soft-contact approach) and R is the equivalent
 376 radius of two particles (a and b) in contact:

377
$$R = \frac{2R_a R_b}{R_a + R_b} \quad (4)$$

378 The interparticle tangent shear stiffness for the Hertzian contact model is defined as:

379
$$k_s = 2 \frac{\sqrt[3]{3G_g^2(1-\nu_g)R}}{2-\nu_g} \sqrt[3]{F_n} \quad (5)$$

380 where F_n is normal contact force.

381 In order to study the effect of stress state, particle shear modulus (G_g), particle Poisson's ratio, (ν_g), and
 382 interparticle friction (μ) on shear wave velocity (V_s), a series of simulations were performed with
 383 different combinations of G_g , ν_g , and μ . In each series, S-wave velocities were measured under different
 384 effective isotropic confining stress levels ranging from 150 kPa to 1200 kPa. The characteristics of each
 385 simulation series are shown in Table 2. In all simulation series, V_s increases as effective mean stress
 386 increases. The slopes of the V_s versus p' curves become smaller as effective stress increases, indicating a
 387 decreasing effect of increasing stress on V_s . This trend is similar to that observed in laboratory tests
 388 (Santamarina et al. 2001; Montoya et al. 2013).

389 **Table 2** Simulation characteristics

Series No.	G_g (GPa)	ν_g	μ	p' (kPa)	α (m/s)	β
T-1 (Iso)	2.9	0.31	0.31	150, 300, 600, 900, 1200	79.50	0.16
T-2 (Iso)	6.0	0.31	0.31	150, 300, 600, 900, 1200	124.95	0.10
T-3 (Iso)	9.0	0.31	0.31	150, 300, 600, 900, 1200	178.01	0.05
T-4 (Iso)	2.9	0.26	0.31	150, 300, 600, 900, 1200	67.28	0.18
T-5 (Iso)	2.9	0.36	0.31	150, 300, 600, 900, 1200	76.85	0.17
T-6 (Iso)	2.9	0.31	0.50	150, 300, 600, 900, 1200	78.60	0.16
T-7 (K ₀)	2.9	0.31	0.31	150, 300, 600, 900, 1200	66.24	0.19

390

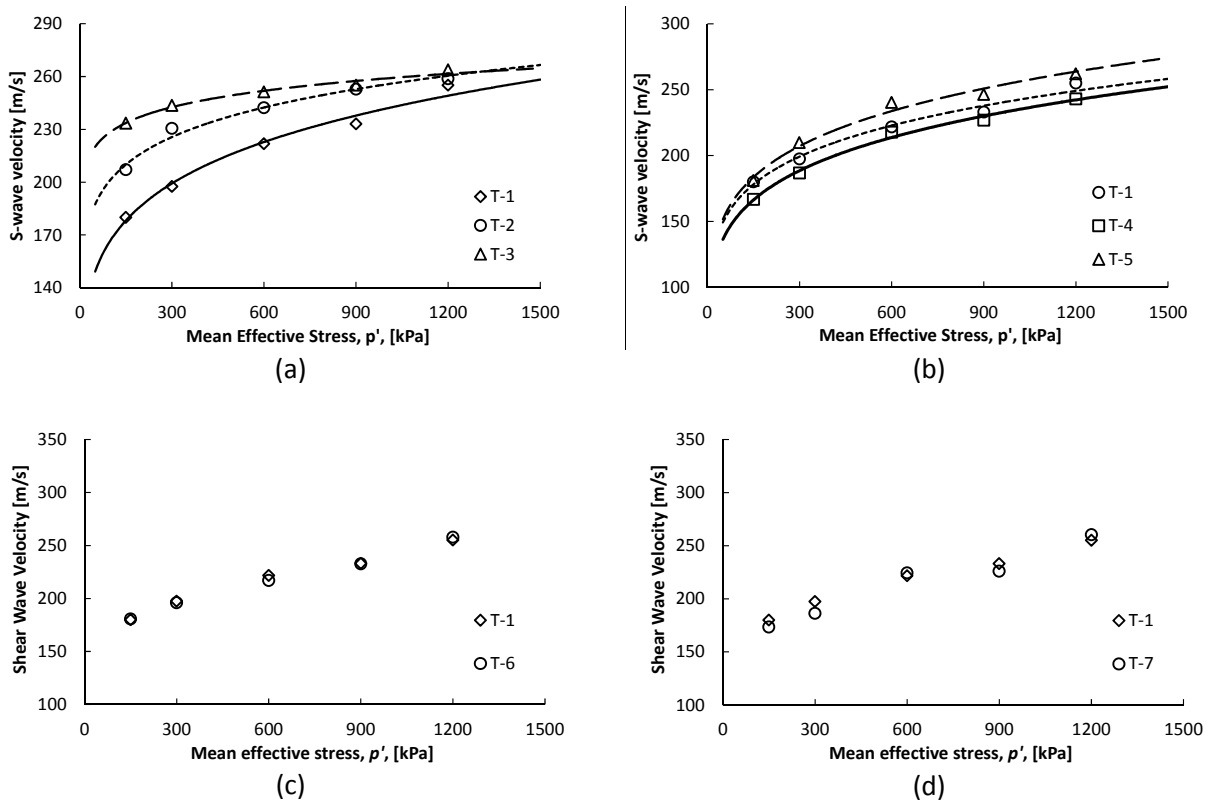
391 Figure 15(a) shows that higher G_g results in higher V_s (reflected by higher α), but lower sensitivity to the
 392 change in stress state (reflected by lower β). Physically, this implies that specimens are more sensitive to
 393 changes in particle stiffness at low mean effective stress than at high mean effective stresses. At higher
 394 mean stress, softer particles have higher contact radii than stiffer particles. Thus, increasing mean stress
 395 leads to improved contact quality (e.g., Yun and Evans 2010) which compensates for the smaller wave
 396 velocity through the individual low-stiffness particles, causing measured velocities to be similar at high
 397 stresses. This behavior is not entirely surprising when the Hertzian normal contact equation for a simple
 398 cubic (SC) packing (Santamarina et al. 2001) is considered:

399
$$\frac{r_c}{R} = \sqrt[3]{\frac{3(1-\nu_g)}{2} \frac{\sigma}{G_g}} \quad (6)$$

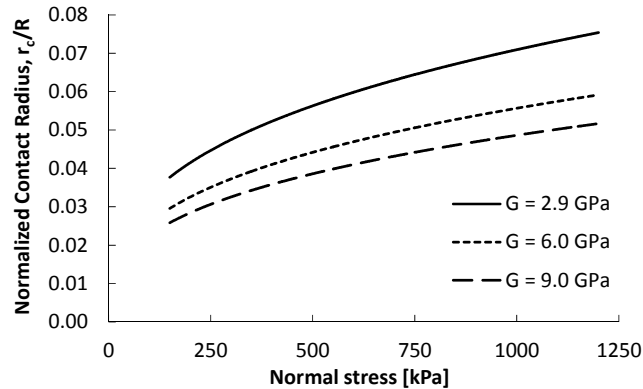
400 where r_c = contact radius, σ = normal stress, and other terms are as previously defined. This expression
 401 clearly shows the nonlinear relationship between contact radius and grain stiffness. The implications of
 402 this relationship for stiffness values considered in the current work are presented in Figure 16, which
 403 shows the more rapid increase in contact radius with increasing stress for the softer particles than the
 404 stiffer particles. Note that if contact area were plotted rather than contact radius, the differences would
 405 be even more pronounced.

406 Figure 15(b) indicates that decreasing v_g results in decreased V_s and vice-versa (note that this is also
 407 consistent with Equation 6). The three V_s versus p' curves are nearly parallel, indicating similar β values.
 408 The effect of interparticle friction, μ , on V_s is shown in Figure 15(c), which implies that V_s is almost the
 409 same for μ values of 0.31 and 0.50. It can be concluded that $\mu = 0.31$ is high enough to avoid sliding in
 410 the assembly and therefore $\mu > 0.31$ has little effect on V_s .

411 The effect of stress state was also investigated. Samples were first isotropically consolidated to a
 412 confining pressure of 50 kPa and then deviatoric stress was applied under K_0 condition until reaching a
 413 desired mean effective stress value. Results shown in Figure 15(d) indicate that the shear wave velocity
 414 is the same for isotropic and K_0 states of stress when mean effective stress is the same. This finding
 415 confirms the validity of equation (2) and is in agreement with the experimental results of Yanagisawa
 416 (1983).



417 **Figure 15.** V_s versus p' . (a) effect of particle shear modulus G_g ; (b) effect of particle Poisson's ratio v_g ; (c) effect of
 418 interparticle friction angle; (d) effect of state of stress. Lines in (a) and (b) represent best fits of Equation (2) to the
 419 data. Fitting parameters are provided in Table 2.



420

421 **Figure 16.** Effects of particle stiffness on Hertzian contact radius for a simple cubic (SC) packing.

422 SUMMARY AND CONCLUSIONS

423 This paper presents a DEM study of S-wave propagation in random assemblies of spherical particles.
 424 DEM simulations provide high quality receiving S-wave signals, given that the responses are free of
 425 interfering factors such as cross-talk, system delay, and environmental noise.

426 The particle motions during wave propagation are illustrated by the evolution of the particle velocity
 427 vector field. Vortex-like disturbances are observed ahead of the main shear motions. From the contours
 428 of shear strain and axial strain, P-wave interference is observed. However, the zone along the central
 429 axis is less affected by P-wave interference. The simulations reveal the complex internal responses of
 430 particulate assemblies subjected to S-wave excitation, in aid of a reasonable and correct interpretation
 431 of S-wave receiving signals.

432 The multiple-receiver configuration in the present simulation makes it possible to calculate S-wave
 433 velocity from the travel time and the distance between receivers. This method produces reliable and
 434 relatively precise results when compared to the S-wave velocity measured directly from the shear wave
 435 lobes shown on the shear strain contours. The study on the cross-correlation method indicates the
 436 length of receiving signal used in cross-correlation method can affect the resulting S-wave velocity,
 437 which should be selected appropriately.

438 S-wave velocity is constant at low excitation amplitude ($\text{amplitude}/D_{50} < 10^{-4}$) and decreases as the
 439 excitation amplitude is further increased. Contact slip is observed when the excitation amplitudes are
 440 high which indicates a transition from elastic to plastic inter-particle response.

441 A wide range of particle sizes are considered. It is found S-wave velocity is effectively size independent
 442 while the resonant frequency under the S-wave excitation shows a linearly decreasing trend in log-log
 443 space as the particle size increases. These results suggest that mass-scaling can be applied in DEM
 444 simulations without altering the resulting S-wave velocity. The excitation frequency should be carefully
 445 selected near the resonant frequency (a function of the particle size) in order to obtain strong frequency
 446 response in the model.

447 The effects of confining stress on S-wave velocity are studied, showing S-wave velocity increases with
448 increasing effective confining stress. The relationship can be described by Eq. (2) which was previously
449 developed based on laboratory tests. Parametric studies on particle shear modulus G_g and particle
450 Poisson's ratio ν_g are performed. It is found that an increase in G_g results in higher α but similar β values
451 while the change in ν_g has minor effects on α and β .

452 ACKNOWLEDGEMENTS

453 The second author has received support from the Jerry Yamamuro Fellowship and the Oregon
454 State University School of Civil and Construction Engineering. This support is gratefully
455 acknowledged.

456 REFERENCES

- 457 Agnolin, I., and Roux, I. (2007). "Internal states of model isotropic granular packings. III. Elastic
458 Properties." *Phys. Rev. E*, (76), 061304.
- 459 Arroyo, M., Muir Wood, D. and Greening, P. D. (2003). "Source near-Field Effects and Pulse Tests in Soils
460 Samples" *Géotechnique*, 53(3), 337-345.
- 461 Belheine N., Plassiard J. P., Donze F. V., Darve F. and Seridi A. (2009). "Numerical simulation of drained
462 triaxial test using 3D discrete element modeling." *Computers and Geotechnics*, 36(1-2), 320-331.
- 463 Blewett, J., Blewett, I. J., and Woodward, P. K. (2000). "Phase and amplitude responses associated with
464 the measurement of shear-wave velocity in sand by bender elements." *Can. Geotech. J.*, 37 1348-
465 1357.
- 466 Burland, J. B. (1989). "Ninth Laurits Bjerrum Memorial Lecture, 'Small is beautiful': The stiffness of soils
467 at small strains." *Canadian Geotechnical Journal*, 26(4), 499-516.
- 468 Clayton, C. R. I. (2011). "Stiffness at small strain: research and practice". *Géotechnique*, 61(1), 5–37.
- 469 Dyvik, R., and Madshus, C. (1985). "Lab Measurements of G_{max} Using Bender Elements." *Advances in the*
470 *Art of Testing Soils under Cyclic Conditions. Proceedings of a session held in conjunction with the*
471 *ASCE Convention*. ASCE, Detroit, MI, Engl, 186-196.
- 472 Evans, T. M., and Frost, J. D. (2007). "Shear banding and microstructure evolution in 2D numerical
473 experiments." *Geo-Denver 2007: New Peaks in Geotechnics, February 18, 2007 - February 21,*
474 *American Society of Civil Engineers, Denver, CO, United states, 28.*
- 475 Evans, T. M., Lee, J., Yun, T. S., and Valdes J. R. (2011). "Thermal Conductivity in Granular Mixtures:
476 Experimental and Numerical Studies." *Deformation Characteristics of Geomaterials*, 815-820.
- 477 Evans, T. M. and Valdes J. R. (2011). "The microstructure of particulate mixtures in one -dimensional
478 compression: numerical studies." *Granular Matter*, 13, 657-669.
- 479 Fam, M., and Santamarina, J. C. (1997). "A study of consolidation using mechanical and electromagnetic
480 waves." *Géotechnique*, 47(2), 203-219.

481 Fernandez, A., and Santamarina, J. C. (2001). "The Effect of Cementation on the Small Strain Parameters
482 of Sands." *Canadian Geotechnical Journal*, 38(1), 191-199.

483 Hardin, B.O., and Richart Jr., F.E. (1963). "Elastic wave velocities in granular soils." *Journal of the Soil
484 Mechanics and Foundations Division*, 89 33-65.

485 Itasca. (2009). "PFC^{3D}: Particle Flow Code in 3 Dimensions." v4.0, Minneapolis, MN.

486 Jacobson, D. E., Valdes, J. R., and Evans, T. M. (2007). "A numerical view into direct shear specimen size
487 effects." *Geotech Test J*, 30(6), 512-516.

488 Lee, J., and Santamarina, J. C. (2005). "Bender elements: Performance and signal interpretation." *J.
489 Geotech. Geoenviron. Eng.*, 131(9), 1063-1070.

490 Li, L., and Holt, R. M. (2002). "Particle scale reservoir mechanics." *Oil and Gas Science and Technology*,
491 57(5), 525-538.

492 Montoya, B. M., DeJong, J. T., and Boulanger, R. W. (2013). "Dynamic response of liquefiable sand
493 improved by microbial-induced calcite precipitation." *Géotechnique*, 63(4), 302-312.

494 Montoya, B. M., Gerhard, R., DeJong, J., Weil, M., Martinez, B., and Pederson, L. (2012). "Fabrication,
495 Operation, and Health Monitoring of Bender Elements for Aggressive Environments." *Geotechnical
496 Testing Journal*, 35(5), 1-15.

497 Ning, Z. and T.M. Evans. (2013). "Discrete Element Method Study of Shear Wave Propagation in Granular
498 Soil." *Proceedings of the 18th International Conference on Soil Mechanics and Geotechnical
499 Engineering*, Paris, France, pp. 1031-1034.

500 O'Sullivan, C. (2011). *Particulate discrete element modelling: a geomechanics perspective*. Taylor &
501 Francis, London.

502 O'Donovan, J., O'Sullivan, C., and Marketos, G. (2012). "Two-dimensional discrete element modelling of
503 bender element tests on an idealised granular material." *Granular Matter*, 14, 733-747.

504 Ouadfel, H. and Rothenburg, L. (2001). "Stress-force-fabric relationship for assemblies of ellipsoids."
505 *Mech. Mater.* **33**, 201-221.

506 Patel, A., Bartake, P. P., and Singh, D. N. (2009). "An empirical relationship for determining shear wave
507 velocity in granular materials accounting for grain morphology." *Geotech Test J*, 32(1), 1-10.

508 Rechenmacher, A.L. (2006). "Grain-scale processes governing shear band initiation and evolution in
509 sands," *Journal of the Mechanics and Physics of Solids*, 54, 22-45.

510 Robertson, P. K., Sasitharan, S., Cunning, J. C., and Segoo, D. C. (1995). "Shear-wave velocity to evaluate
511 in-situ state of Ottawa sand." *J. Geotech. Eng.*, 121(3), 262-273.

512 Sadd, M. H., Tai, Q., and Shukla, A. (1993). "Contact law effects on wave propagation in particulate
513 materials using distinct element modeling." *Int. J. Non-Linear Mech.*, 28(2), 251-65.

514 Sanchez-Salinero, I., Roesset, J. M., and Stokoe, K. H. (1986). "Analytical studies of body wave
515 propagation and attenuation." *Rep. No. Report GR 86-15*, University of Texas, Austin.

516 Santamarina, J.C., in collaboration with Klein, K. and Fam, M. (2001). *Soils and Waves*, J. Wiley and Sons,
517 Chichester, UK, 488 pages.

518 Santamarina, J.C. and Fratta, D. (2005), "Discrete Signals and Inverse Problems An Introduction for
519 Engineers and Scientists". J. Wiley and Sons, Chichester, UK, 350 pages.

520 Saxena, S. K., Avramidis, A. S., and Reddy, K. R. (1988). "Dynamic moduli and damping ratios for
521 cemented sands at low strains." *Can. Geotech. J.*, 25(2), 353-368.

522 Sharma, R., Baxter, C., and Jander, M. (2011). "Relationship between shear wave velocity and stresses at
523 failure for weakly cemented sands during drained triaxial compression." *Soils and Foundations*,
524 51(4), 761-771.

525 Shirley, D. J., and Hampton, L. D. (1978). "Shear-Wave Measurements in Laboratory Sediments." *J.*
526 *Acoust. Soc. Am.*, 63(2), 607-613.

527 Styler, M. A., and Howie, J. A. (2012). "Comparing frequency and time domain interpretations of bender
528 element shear wave velocities." *GeoCongress 2012*, ASCE, Oakland, California, 2207-2216.

529 Tordesillas, A., Muthuswamy, M., and Walsh, S. (2008). "Mesoscale Measures of Nonaffine Deformation
530 in Dense Granular Assemblies." *J. Eng. Mech.*, 134(12), 1095-1113.

531 Viggiani, G., and Atkinson, J. H. (1995). "Interpretation of bender element tests." *Géotechnique*, 45(1),
532 149-154.

533 Woodcock, N.H. (1977). "Specification of fabric shapes using an eigenvalue method". *Geol. Soc. Amer.*
534 *Bull.* 88, 1231-1236.

535 Yanagisawa, E. (1983). "Influence of void ratio and stress condition on the dynamic shear modulus of
536 granular media". in J. T. Jenkins and M. Satake (eds), *Advances in the Mechanics and Flow of*
537 *Granular Materials*, Elsevier, Amsterdam, 947-960.

538 Yang, J., and Gu, X. Q. (2012). "Shear stiffness of granular material at small strains: does it depend on
539 grain size." *Géotechnique*, 63(2), 165-179.

540 Yun, T. S., and Evans, T. M. (2010). "Three-dimensional random network model for thermal conductivity
541 in particulate materials." *Computers and Geotechnics*, 37(7-8), 991-998.

542 Zhao, X., and Evans, T. M. (2009). "Discrete simulations of laboratory loading conditions." *International*
543 *Journal of Geomechanics*, 9(4), 169-178.

544